Role of Meniscus Shape on Crystallization of Molecular Semiconductors and Fluid Dynamics During Meniscus-Guided Coating

Okan Yildiz, Zuyuan Wang, Mateusz Brzezinski, Shuanglong Wang, Zhenpeng Li, Jasper J. Michels, Paul W. M. Blom, Wojciech Pisula,* and Tomasz Marszalek*

Meniscus-guided coating (MGC) is a promising method that offers predictable fabrication of highly crystalline thin films. For the integration of molecular semiconductors into large-area electronic devices with high efficiency and reliability, homogeneous and highly ordered film morphologies are required. The solution processing of such defect-free film structures requires comprehensive understanding of the complex relationship between molecular crystallization, fluid dynamics, and meniscus shape. In this work, the role of the meniscus shape on fluid dynamics in the coating bead and the crystallization process of the low molecular weight semiconductor 6,13-bis(triisopropylsilylethynyl)pentacene (TIPS-pentacene) during zone-casting is systematically investigated. Depending on meniscus shape and coating velocity, four morphological subregimes are found: stick-slip morphology, unidirectional homogenous crystal stripes, spherulitic morphology, and directional branched morphology; of which the second exhibits the highest crystallinity with a reduced trap density in the thin film, resulting in improved saturation and effective mobilities in field-effect transistors (FET). Numerical simulation of fluid dynamics explains the observed morphological trends, which are correlated with the electrical behavior of the devices. This work provides a fundamental basis for upscaling MGC methods for the application of functional thin films.

1. Introduction

Controlling morphology and molecular packing of organic semiconductor (OSC) films are important for achieving high-performance organic field-effect transistors (OFETs).[1] Solution-processing has gained tremendous attention for the deposition of highly crystalline OSC films due to its low costs, scalability,[2,] and crystallinity control.[3] There are still challenges for large-area solution processing. These difficulties are mainly related to structural defects such as film discontinuity, morphological irregularities, grain boundaries, and small grain sizes, which directly affect the electrical performance of OSC films.[3] One common laboratory technique is spin-coating, which is not effective for large-area film fabrication due to significant material waste and incompatibility with upscaling. Furthermore, due to a non-uniform shear stress distribution precise control over the film morphology is compromised with this technique.[4] Unlike other solution coating methods, meniscus-guided coating (MGC) techniques such as solution-shearing,[5] dip-coating,[6] bar-assisted meniscus shearing[7] and zone-casting[8] allow controlling the film morphology, the film dimensions such as thickness, width, length and the molecular packing. The MGC techniques are based on the formation of a solution meniscus on a moving substrate. The substrate moves at a constant speed as the solvent evaporates,

O. Yildiz, M. Brzezinski, S. Wang, J. J. Michels, P. W. M. Blom, W. Pisula, T. Marszalek
Max Planck Institute for Polymer Research
Ackermannweg 10, 55128 Mainz, Germany
E-mail: pisula@mpip-mainz.mpg.de; marszalek@mpip-mainz.mpg.de

Z. Wang, Z. Li
School of Mechanical and Electrical Engineering
University of Electronic Science and Technology of China
Chengdu, Sichuan 611731, China
W. Pisula, T. Marszalek
Department of Molecular Physics
Faculty of Chemistry
Lodz University of Technology
Zeromskiego 116, Lodz 90-924, Poland

2314131 (1 of 10)

**ADVANCED
SCIENCE NEWS**

www.advancedsciencenews.com

**ADVANCED
FUNCTIONAL
MATERIALS**

www.afm-journal.de
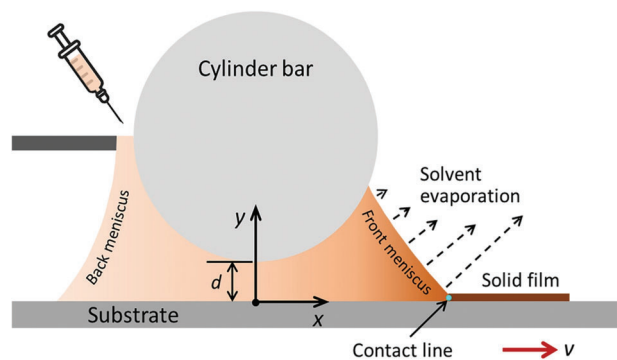
Figure 1. A schematic illustration of the meniscus during zone casting with the solute concentration field. The deposition head is formed between a cylinder bar and a substrate, which are separated by a gap distance of d. The front meniscus shows predominant solvent evaporation as the substrate moves at a coating speed of v.

forming a solid film in a unidirectional fashion as shown in **Figure 1**.[2,4,6,9]

To control the thin film morphology during MGC, the individual process parameters and their coupling have been studied.[4] These parameters include the choice of solvent,[9a,b] solute concentration,[10] coating velocity,[3,9d,11] deposition temperatu[9a] surface treatment of the substrate[12], and the gap distance between the coating bead and the substrate. Particularly, the evaporation-induced concentration gradient at the meniscus contact line as seen in Figure 1 is crucial for the formation of the thin film morphology. For instance, the film roughness of MGC films greatly varies, depending on the relation between the boiling temperature of the solvent T_b and the deposition temperature T. As T increases and approaches T_b, the concentration gradient increases, resulting in a smoother surface film morphology.[9a] Second, an optimized solute concentration (c_S) of 0.4 wt.% TIPS-pentacene in hexane after MGC results in few structual defects and therefore in improved charge carrier mobility and lowered contact resistance at the metal electrode / OSC interface of the OFET device.[10] Our previous work has shown that c_s should also be optimized toward the coating velocity v because of morphological transitions at different v.[9d] Such morphological transitions occur at a critical coating velocity that increases with solute concentration.[9d] Moreover, limited mass transport at the contact line results in misaligned OSC crystals with respect to the coating direction. One solution to this problem is to design a coating head that allows for enhanced mass transport toward the contact line, thereby influencing the crystallization of OSC solute. Enhanced fluid flow provides a better crystal alignment and low device-to-device variation in OFET performance.[5,11]

Another way to exert control is by tuning the gap distance d between the coating head and the substrate, as it influences the shape of the meniscus, as we will show below. The number of studies in the present literature that include the gap distance as an optimization parameter for MGC is small. This is perhaps surprising, as, in particular for advanced methods such as zone-casting and slot-die coating, the gap distance seems to be a readily accessible parameter for exerting control. Born et al. studied the influence of the gap distance of the meniscus on the film formation of polystyrene microparticles from solution during MGC.

At 160 μm a stable meniscus was obtained, whereas a larger gap distance resulted in an increase in the depinning length (a maximum displacement) of the contact line, resulting in an inhomogeneous distribution of the microparticles and a strongly deformed film.[13] In another example, the meniscus shape was controlled by dip-coating C8-BTBT by tilting the substrate at different angles with respect to the surface of the liquid.[6] As shown by numerical simulations, the concentration gradient at the contact line becomes steeper with a decreasing tilt angle, which leads to enhanced coverage and crystallinity of the film. The effect of the meniscus shape, as determined by the gap distance, on the fluid dynamics in the coating bead remains poorly understood and has so far not been systematically studied in the case of a crystallizing small molecular solute. For that reason, at present no guidelines exist for attaining further process control through optimizing the gap distance.

In this work, we account for this and investigate the role of the meniscus shape by systematically varying the gap distance during zone-casting of TIPS-pentacene as a highly crystalline model semiconductor. We study how the gap distance affects the fluid dynamics in the bead, as well as the thin film morphology. At a given coating velocity in the evaporative coating regime, upon decreasing the gap distance we identify a transition from a morphology characterized by periodic ridges that extend perpendicular to the coating direction toward a favorable morphology comprising unidirectionally aligned crystal domains. Upon entering the hydrodynamic coating regime (i.e., commonly known as Landau–Levich regime and also partially dominating the transition between the evaporation and Landau–Levich regimes)[4,14] at a high coating velocity, we observe an isotropic spherulitic morphology for a large gap distance, which transforms in a more directional, branched structure when the gap distance is decreased. Numerical simulation of the steady state fluid flow pattern in the bead provides information about the impact of the meniscus shape on the concentration and temperature gradients in the coating bead. Finally, we show that the favorable directionality and considerable grain size in the aligned morphology II leads to a low trap density, giving optimal OFET performance in terms of saturation and effective mobility.

2. Results and Discussion

Figure 1 gives a schematic representation of the zone-casting process (belonging to the group of meniscus-guided coating methods), including the deposition head geometry, the gap distance d, and the concentration field.[9d] As the substrate moves at a constant velocity v, the solvent evaporates dominantly at the front meniscus and the solute accumulates toward the contact line of the front meniscus. During deposition, a continuous solution supply is provided via the inlet to maintain a stable bead with a constant volume. As shown by numerical simulations in previous work,[9d] the flow pattern in our set-up typically comprises two vortices, resulting from the inlet solution supply, substrate entrainment, and solvent evaporation. At low coating velocities (i.e., in the evaporative regime), the deposited film crystallizes immediately adjacent to the contact line. At substantially higher coating velocities, the film crystallization generally occurs further downstream from the contact line.[4,9b,14a]
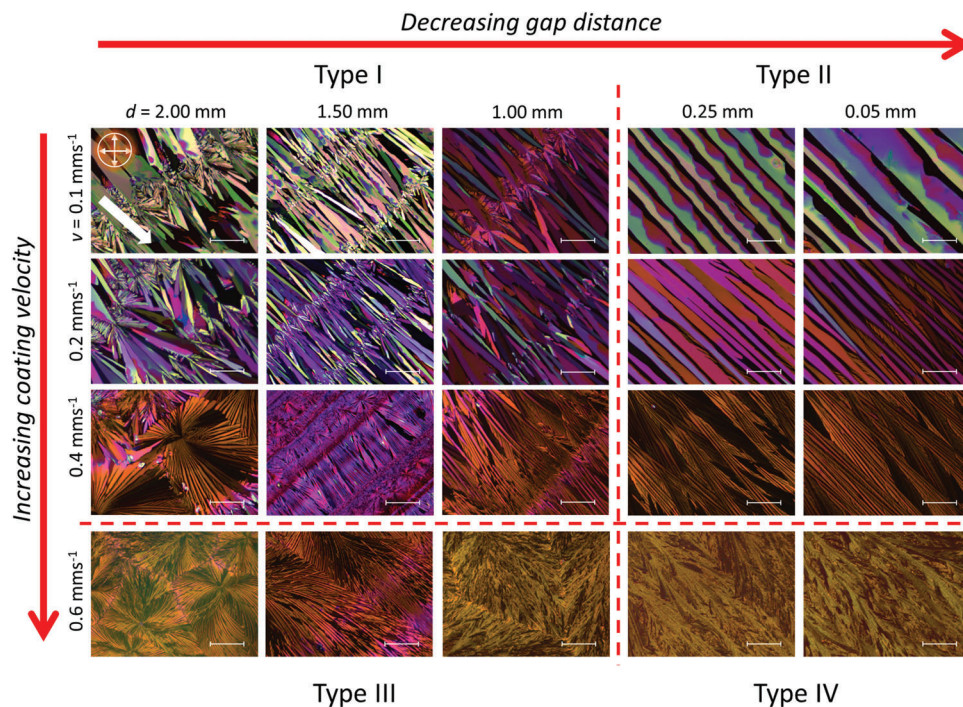
Figure 2. POM images of zone-cast TIPS-pentacene films deposited at the gap distances d = 2.00, 1.50, 1.00, 0.25, and 0.05 mm and coating velocities v = 0.1, 0.2, 0.4, and 0.6 mm s^{-1}. The white arrow and the crossed arrows in the first image indicate the coating direction and the position of two polarizers, respectively. Three morphological subregimes separated with red dashed lines are indicated. All scale bars are 50 µm.

In this study, we chose TIPS-pentacene as a model compound for the zone-casting experiments. TIPS-pentacene is known to exhibit a high crystallinity and the ability to form unidirectionally aligned crystals, owing to its brick-wall packing and long-range molecular arrangements.[3,11,15] The compound was dissolved in tetrahydrofuran (THF) at a concentration of 1.00 mg mL^{-1}. Five different gap distances in the range $0.05 \leq d \leq 2.00$ mm were set to control the meniscus shape at four different coating velocities in the range $0.1 \leq v \leq 0.6$ mm s^{-1}. The coating velocities were selected within the "optimized window", as described in our previous work[9d], and represent the evaporative regime, with the upper limit extending into the transition toward the Landau–Levich regime. In this velocity window, we observed unidirectionality and homogeneous alignment in thin films of the semiconductor C8-BTBT, which behaves similarly to TIPS-pentacene when applied by MGC.[3,16] The morphology of the deposited films was characterized by polarized optical microscopy (POM) and atomic force microscopy (AFM).

The POM images in **Figure 2** reveal four types of crystalline morphologies resulting from the interplay between the gap distance d and the coating velocity v. In general terms we observe: I) "interrupted unidirectional bands" for a high d and a low v, II) "uninterrupted unidirectional bands" for a low d and a low v, III) spherulites for a high d and a high v, and IV) a "directional branched" structure for a low d and a high v. The directionality in morphologies I, II, and IV aligns with the coating direction (white arrow), expressing principle control over crystal growth in the evaporative and transition regimes.[9d] Close inspection of morphology I reveals that the "interruptions" are in fact ridges that extend perpendicular to the coating direction, comprising

small needle-like crystals that, in contrast to the bands in the intermittent regions, do not seem to have a particular directionality. The periodicity of the irregularity exhibits a qualitative reciprocal relation with the gap distance and disappears at the transition I→II. Below we propose an origin for the ridges in morphology I with the aid of numerical simulations of the fluid dynamics in the coating bead, taking into account the non-uniform temperature distribution.

Both morphology types I and II reveal a gradually decreasing crystal bandwidth from ≈30 to ≈3 µm when v is increased from 0.1 to 0.4 mm s^{-1} (Figure 2). We observed the same effect for zone-cast films of C8-BTBT.[9d] In principle, each crystal stripe represents a nucleation center and a higher v increases the nucleation density due to the enhanced concentration gradient, and higher supersaturation near to the contact line, giving rise to narrower bands.[9d] When v is increased to 0.6 mm s^{-1}, a spherulitic morphology or directional branched structure emerge (types III and IV). For a gap distance of $d < 0.25$ mm, the structure in the type IV morphology still follows the coating direction. This is an important observation from an application point-of-view, as effective production requires control at a maximum coating velocity. However, at a higher gap distance the orientation is lost and the domains become isotropic (Morphology III). Besides POM analysis, atomic force microscopy (AFM) was performed to evaluate the surface roughness (RMS) and average grain size of the deposited thin films. At $d = 0.05$ mm, the lowest RMS were obtained of ≈15 nm at 0.1 mm s^{-1} and ≈7 nm at 0.6 mm s^{-1} (Figure S1g, Supporting Information). Increasing the gap distance to 1.00 and 2.00 mm caused a gradual increase in the RMS roughness of the thin films for type I and II morphologies. As also shown in

**ADVANCED
SCIENCE NEWS**

www.advancedsciencenews.com

**ADVANCED
FUNCTIONAL
MATERIALS**

www.afm-journal.de

Figure S1g (Supporting Information), the largest grains ($\approx$260 μm^2) were produced at $d = 0.05$ mm and $v = 0.1$ mm s^{-1} and decreases to $\approx$33 μm^2 at $d = 2.00$ mm. On the other hand, the average grain size at $v = 0.6$ mm s^{-1} remains almost constant with respect to the gap distance for type III morphology.

Next, we focus on the origin of the perpendicular ridges that appear in Morphology I. The fact that the needle-like crystals in these ridges (see Figure 2) grow isotropically suggests that the contact line is temporarily, but periodically, stationary relative to the substrate. In other words, it temporarily moves along with the substrate rather than sliding across it, implying that unidirectional control is lost for a small-time interval. This mechanism is consistent with the phenomenon that under the influence of Marangoni stress the meniscus may exhibit a hydrodynamic instability which causes it to periodically bulge into the coating direction.[17] This instability stems from the surface tension gradients along the coating direction, which may be induced by local variation in composition and/or temperature. As evidence, we added to the supporting information two real-time videos recorded during zone-casting. V1 shows that the front meniscus bulges periodically forward and backward during the deposition at high gap distance ($d = 2.00$ mm, $v = 0.1$ mm s^{-1}). In contrast, a higher stability at the dynamic evaporation of the solvent is established during the deposition at small gap distance ($d = 0.05$ mm, $v = 0.1$ mm s^{-1}) as shown in V2. Since in the evaporative coating regime, the solute concentration remains very low in the bead, except near the contact line, we deem temperature gradients to be the primary origin for the Marangoni flow. To confirm the insignificance of the solutal Marangoni effect, we conducted surface tension measurements on TIPS-pentacene / THF solutions with concentrations of $c_0 = 1.56$ mol m^{-3} and $c_1 = 15.6$ mol m^{-3} (see Figure S2, Supporting Information). The fact that the surface tensions of both solutions are the same within the experimental error corroborates our choice of neglecting the solutal Marangoni effect. A more detailed explanation is given in Section S2 (Supporting Information).

To support the hypothesis that a periodic Marangoni stress-induced meniscus instability may be the cause for the formation of the ridges, we performed 2D numerical simulations that clearly show the presence of a temperature gradient across the meniscus, which could give rise to the aforementioned instability, though without directly modeling the actual deformation of the fluid-vapor interface itself. These steady-state numerical continuum simulations include fluid flow, temperature, and concentration fields in the coating bead in the low-speed regime[9d,f,18] at varying gap distances ($d = 0.05$, 1.00, and 2.00 mm) and coating velocities ($v = 0.1$–0.6 mm s^{-1}). We solved the Navier–Stokes (NS) equations, in conjunction with the convection-diffusion equations for heat and concentration, while accounting for the thermal Marangoni effect. The considered material system is a solution of TIPS-pentacene (solute) in THF (solvent) with a concentration of $c_0 = 1.56$ mol m^{-3} at the inlet. Considering the low solute concentration in the coating bead (except for the region near the contact line), we adopted the THF properties as the solution properties (including the density, viscosity, specific heat, thermal conductivity, surface tension, and enthalpy of vaporization, see Figure S3, Supporting Information), and took the temperature dependence of these properties into account. The shape of the simulation box was physically pre-determined and

fixed to match the shape of the actual coating bead.[9d] As was done in our previous work,[9d,10,19] we cut a small region near the contact line of the front meniscus to explicitly allow the solution to exit the simulation domain upon entrainment. In agreement with the experiments, the solute concentration at the inlet was fixed at $c_0 = 1.56$ mol m^{-3}, and the temperatures of the substrate, cylinder bar, and inlet solution were set to be constant at 45 °C. The boundary condition at the outlet was set to be "outflow". At the substrate no-slip conditions were assumed. Solvent evaporation was assumed to occur primarily at the front meniscus and negligible at the back meniscus. The evaporation rate j was assumed to be $j(x) = A/[(x_{tip} - x + B)/1[\mu m]]^{1.5}$, which ensures an escalation in the evaporation rate toward the contact line of the front meniscus, characteristic to coating in the evaporative regime. Similar to our previous work,[9d] we chose $B = 1$ μm and iteratively determined $A = 7.6555 \times 10^{-3}$ m s^{-1} by imposing mass conservation of the solvent in the cut region (i.e., the total solute flux at the inlet is equal to that at $x = x_{cut}$, while the total solvent flux at the inlet is equal to that at the front meniscus and $x = x_{cut}$). The deposited film thickness was obtained by equating the solute mass flux at the inlet and outlet via $h = v^{-1} \int_0^{\gamma_{cut}} u(\gamma)\phi(\gamma)d\gamma$, where $u(\gamma)$ and $\phi(\gamma)$ are the substrate velocity and solute volume fraction at the position of the cut.[9d]

Figure 3a illustrates the simulation domain, boundary conditions, and coordinate system, as well as exemplary flow, and temperature fields at $d = 0.05$ mm and $v = 0.6$ mm s^{-1}. The combined effects of the inlet solution supply, substrate entrainment, solvent evaporation, and thermal Marangoni flow lead to unique streamline distributions that feature four vortices in the simulation domain and one stagnation point at the front meniscus. At the stagnation point the local fluid velocity is zero, effectively separating downstream flow and upstream backflow patterns. The zoomed-in image (a1) in Figure 3a shows a local low-temperature region due to the strongly enhanced solvent evaporation near the contact line, whereas the zoomed-in image (a2) depicts the aforementioned cut region that allows the solute to leave the simulation box.

Figure 3b,d shows the solute concentration fields together with the corresponding flow streamlines at $d = 0.05$, 1.00, and 2.00 mm, respectively. As d increases from 0.05 to 1.00 mm, the number of vortices decreases from four to three; as d further increases to 2.00 mm, the relative sizes of the three vortices change. In all cases, the solute concentration considerably increases toward the contact line, with the size of the high-solute-concentration region decreasing with the gap distance. In contrast to ref. [18], where the temperature gradient-induced thermal Marangoni flow hinders the delivery of solution to the contact line at the front meniscus, the thermal Marangoni effect in our coating bead promotes the solution delivery to the contact line, as indicated by the direction of the streamlines in the vortex near the contact line.

For each of the three gap distances, we varied v from 0.1 to 0.6 mm s^{-1} and studied the film thickness h. As evident from Figure 3e, similar thickness values are obtained for gap distances of 0.05 and 1.00 mm. At a larger d of 2.00 mm, h increases due to enhanced solvent evaporation in the front meniscus. A similar trend for the dependence of the film thickness on the meniscus gap was observed previously for phospholipids deposited by

2314131 (4 of 10)
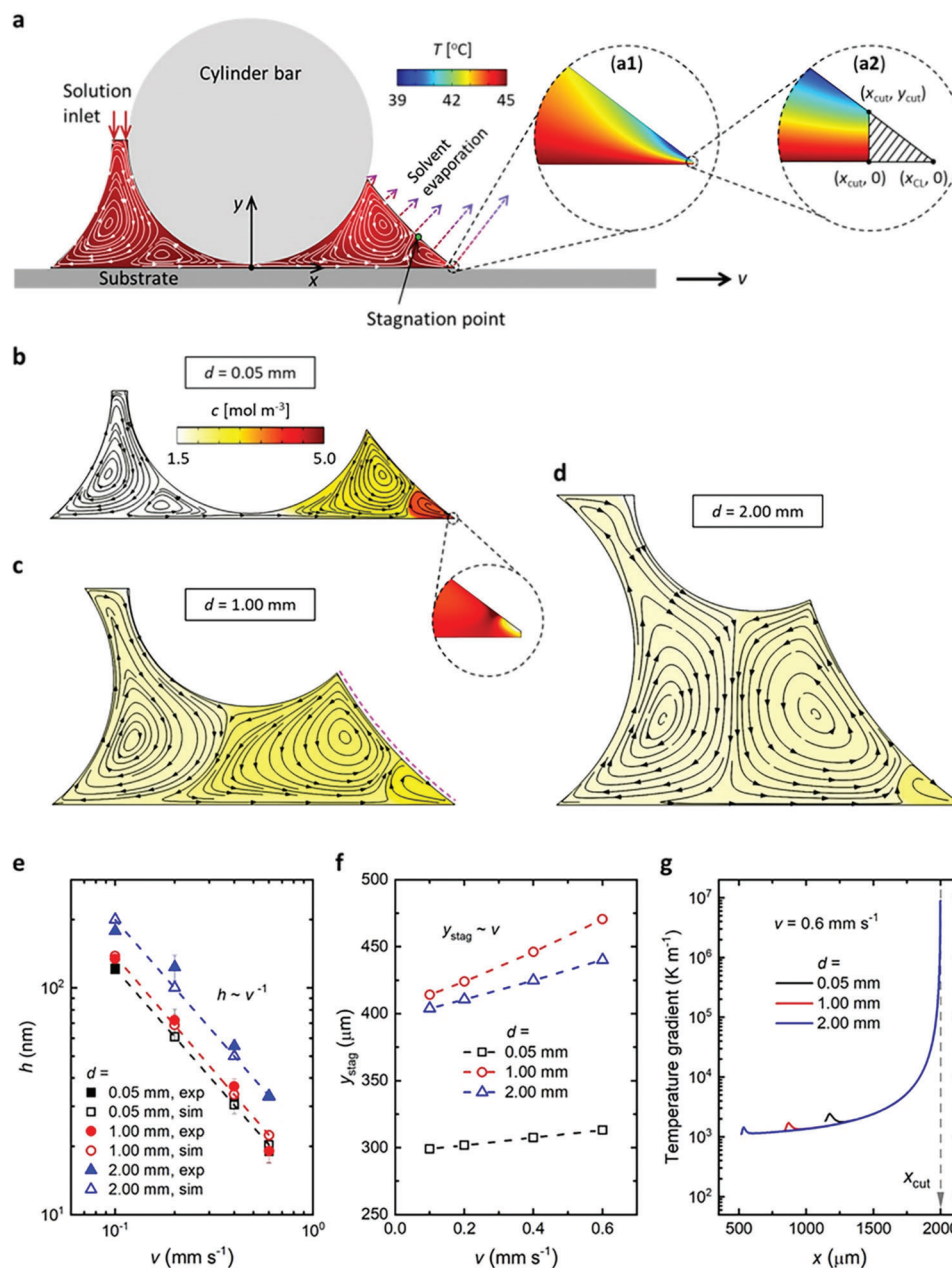
Figure 3. Finite element simulations of the flow, temperature, and concentration fields in the meniscus during zone-casting of TIPS-pentacene. a) Illustration of the simulation domain, boundary conditions, and coordinate system. The strong solvent evaporation near the contact line results in a local low-temperature region [zoomed-in image (a1)]. A small region near the contact line is cut to allow the solute to leave the simulation domain [zoomed-in image (a2)]. Flow and concentration fields for b) $d = 0.05$ mm, c) $d = 1.00$ mm, and d) $d = 2.00$ mm. The results in (a–d) correspond to $c_0 = 1.56$ mol m^{-3} and $v = 0.6$ mm s^{-1}. e) Experimental and calculated film thicknesses h as a function of the casting speed v at three gap distances. f) y coordinate of the stagnation point (see (a)) as a function of the casting speed v at three gap distances. g) Temperature gradient along the front meniscus [see the magenta dashed curve in (c)] as a function of the x coordinate for three gap distances. The casting speed dependence of the temperature gradient is negligible.

MGC.[14a] At a constant v, h increases with d (Figure 3e), suggesting that the film thickness is closely affected by the fluid flow in the front meniscus due to d. At a constant d, h decreases with increasing v, following a trend consistent with the $h \sim v^{-1}$ relation, characteristic for the evaporative regime. It has been shown in literature that the relation $h \sim v^{-1}$ can be obtained by simply equat-

ing the outgoing fluxes of the solvent (evaporation) and solute (solidification) to the influx of the native solution.[6,9d,10,19] The theoretical thicknesses calculated by the numerical simulations are in excellent agreement with the experimental data at all three gap distances (Figure 3e). Because validation of the numerical model by only using the dry film thickness is not fully sufficient,

**ADVANCED
SCIENCE NEWS**

www.advancedsciencenews.com

**ADVANCED
FUNCTIONAL
MATERIALS**

www.afm-journal.de

we extended our model to include flow velocity, and distribution of temperature and concentration (Figure 3a–g), similar to previous studies.[9d,f]

As the solvent evaporation occurs primarily at the front meniscus, the solute concentration in the coating bead remains virtually independent of v and close to the inlet concentration c_0, except in the region near the contact line, where the solute concentration drastically rises due to the diverging evaporation rate.[6,9d,10] Since the stagnation point (y_{stag}) at the front meniscus, which defines a point where the upstream and downstream flows split (Figure 3a), is an important feature of the flow field, we have studied its dependence on the gap distance and coating velocity. As shown in Figure 3f, y_{stag} increases linearly with v at a constant d and shows a prominent jump as d is increased from 0.05 to above 1.00 mm. Because the downstream flow transports the solute to the contact line, y_{stag} (or the size of the downstream region below the stagnation point) seems crucial for the crystallization process.[6,9d,f] Interestingly, the smaller y_{stag} values at $d = 0.05$ mm (Figure 3f) correspond to the smaller film thicknsses (Figure 3e), as compared to the situations at $d = 1.00$ and 2.00 mm. In Figure 3g, we show the temperature gradients along the front meniscus as a function of x for the three gap distances at $v = 0.6$ mm s^{-1} (the v-dependence of the temperature gradients was found to be negligible). Surprisingly, the temperature-gradient versus x profiles are nearly identical at the three gap distances, suggesting a weak dependence of the thermal Marangoni effect on the gap distance. The temperature distribution as represented by the variable color in Figure 3a indicates significant temperature changes mainly close to the contact line at the front meniscus. This is due to the predominant solvent evaporation causing cooling (blue color) at the front meniscus. Therefore, the numerical simulations help elucidate the influences of the gap distance and coating velocity on the film thickness and the flow (e.g., vortices, stagnation point), temperature (e.g., temperature, temperature gradient), and solute concentration fields in the bead.

Next, we outline how our simulations, despite not allowing for deformation of the meniscus, are consistent with the formation of periodic "ridges" normal to the coating direction, as seen in the POM images of films obtained at high gap distances and low coating velocities (Figure 2). According to Figure 3g, the temperature gradient, and hence an associated Marangoni stress, is comparable for all three gap distances. On the other hand, a higher gap distance means a larger vertical distance from the substrate to the front meniscus, for example, from the substrate to the stagnation point. It is clear that a larger y_{stag} (at a larger gap distance) together with a lower coating velocity gives a smaller velocity gradient from the substrate up to the free surface of the front meniscus. Therefore, both increasing the gap distance and lowering coating velocity reduce the shear rate in the region close to the contact line at the front meniscus, which weakens the viscous entrainment by the substrate.

We propose that the thermal Marangoni effect counteracts the stabilizing effect of viscous entrainment. When the latter dominates over the former (i.e., at small d's and/or large v's), uniform solid films are formed; otherwise, "ridges" normal to the coating direction start to appear, originating from a periodic hydrodynamic instability similar to the one described by Doumenc et al.,[17] here driven by thermal Marangoni stress (see Videos S1

and S2, Supporting Information). We support this reasoning as follows. The stabilizing effect by viscous forces is shown in the mentioned report,[17] where the instability is suppressed by either raising the solution viscosity (e.g., via increasing the solute concentration) or by increasing the coating velocity. Either measure would increase the local shear stress according to $\tau = \eta\dot{\gamma}$, with $\dot{\gamma} = v/d$ the shear rate. Doumenc and Guerrier's report[17] does not include gap distance, but the fact that the shear rate increases with decreasing d, that is, $\dot{\gamma} = v/d$, with a concomitant observed disappearance of the ridges, suggests that with decreasing gap distance the viscous stress (locally) increases, possibly overcoming Marangoni stress, thereby providing a stabilizing effect that suppresses the instability.

Besides the changes in the film morphology of TIPS-pentacene, we further evaluate the UV–vis absorption. To make a comparison between the thin films, we examine the absorption peak ≈365 nm (≈3.4 eV) which corresponds to LUMO level of TIPS-pentacene.[19] The absorption peak ≈365 nm (3.4 eV) is blueshifted by ≈7.0 nm for the gap distance of 2.00 mm in comparison to 0.05 mm at both of coating velocity of 0.1 mm s^{-1} (**Figure 4a**) and 0.6 mm s^{-1} (Figure 4b). The spectral change is a sign for differences in the crystal packing of TIPS-pentacene and indicates that the required energy to excite the valence electrons shifts by ≈0.07 eV together with the morphological transition. Similarly, spectral changes were observed for C8-BTBT films obtained by off-center and on-center spin-coating.[20] The spectral shift to lower wavelengths implies a lower film crystallinity, as in the case for the gap distance of 2.00 mm. This observation is in agreement with the higher crystallinity for films deposited at lower gap distance. Furthermore, films obtained at 0.05 and 1.00 mm gap distances show similar absorption peaks at ≈365 nm for coating speeds of 0.1 and 0.6 mm s^{-1} indicating less disturbed intermolecular interactions and molecular packing at 1.00 mm compared to 2.00 mm. The peak related to the LUMO level of TIPS-pentacene is blueshifted only for the film coated at gap distance of 2.00 mm. The bulging of the meniscus seems to disrupt the crystallization more at 2.00 mm gap distance compared to 1.00 mm.
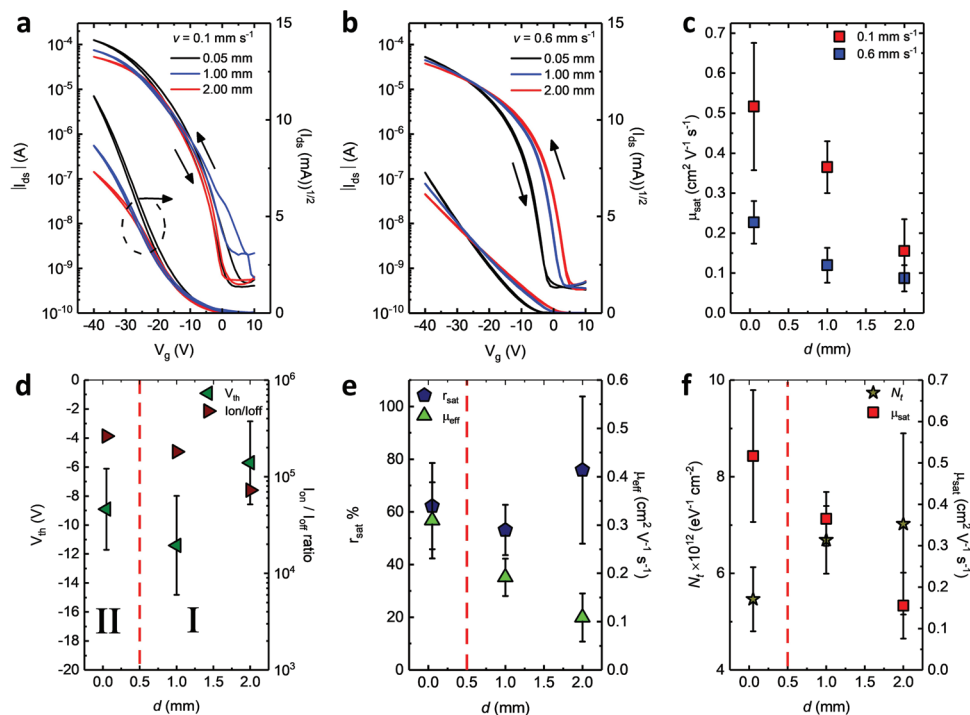
To investigate the dependence of the fluid flow on the molecular organization, grazing incidence wide-angle X-ray scattering (GIWAXS) measurements were performed. Six different morphologies were analyzed and obtained at gap distances of 0.05, 1.00, and 2.00 mm and coating velocity of 0.1 and 0.6 mm s^{-1} (Figure 2). The GIWAXS patterns are presented in Figure S4 (Supporting Information) and display the diffraction peaks of the TIPS-pentacene ordering in out-of-plane and in-plane directions. The thicker films result in higher scattering intensities in the GIWAXS patterns in case of a coating velocity of 0.1 mm s^{-1} (Figure S4a–c, Supporting Information). As previously reported,[3] TIPS-pentacene forms brick-wall packing as shown in Figure 4c. The Miller indices (001) and (100) are attributed to the out-of-plane and in-plane directions as also indicated by the arrows in Figure 4c. The highest peak intenstiy is related to the interlayer distance (001) in all cases. The relation between the interlayer distance and the gap distance at two different coating velocities is given in Figure 4d. At processing conditions of $d = 0.05$ mm and $v = 0.1$ mm s^{-1} an interlayer distance of 16.1 Å is determined from the (001) peak in Figure S4 (Supporting Information). This distance slightly
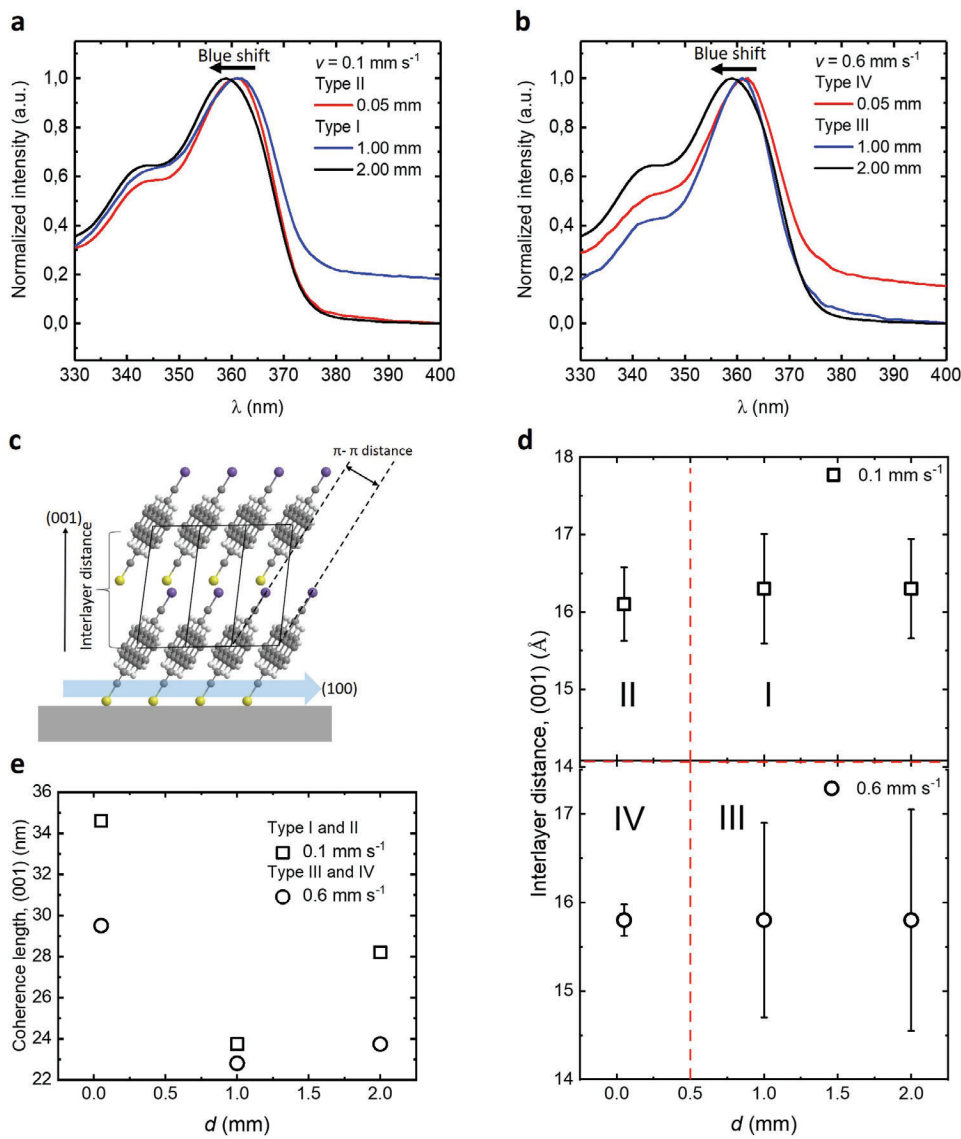
Figure 4. UV–vis absorption of zone-cast TIPS-pentacene films for a) $v = 0.1$ mm s^{-1} with morphology type II ($d = 0.05$ mm) and type I (1.00 and 2.00 mm) and b) $v = 0.6$ mm s^{-1} with the morphology type III (1.00 and 2.00 mm) and type IV (0.05 mm). c) Side view of the molecular packing of zone-cast TIPS-pentacene. The miller indices (001) represent the out-of-plane direction and (100) represents the in-plane direction. Blue arrow indicates the casting direction. The interlayer distance d) and the coherence length of (001) peak e) are shown as a function of gap distance for the coating velocities of 0.1 and 0.6 mm s^{-1}.

increases to 16.3 Å for 1.00 and 2.00 mm at the same coating speed. At these two gap distances, a second diffraction peak appears marked (001)* in Figure 4, corresponding to a distance of 15.8 Å, indicating the formation of polymorphs. Upon increasing the speed to 0.6 mm s^{-1}, the interlayer distance in the main crystal phase decreases to 15.8 Å for $d = 0.05$ mm. For $d = 1.00$ and 2.00 mm at 0.6 mm s^{-1}, the two (001) and (001)* peaks are also observed, and the peak variation increased to ≈2 Å. The molecular arrangement in the out-of-plane direction was found to be dependent on meniscus shape and coating velocity, and hence on the fluid flow. The type II morphology cast at the gap distance of 0.05 mm reveals a homogenous molecular ordering in the out-of-plane direction as proven by a single (001) diffraction peak.

To better understand the role of zone-casting conditions on the crystallinity of TIPS-pentacene, we evaluated the coherence length (or crystallite size) using the Scherrer equation.[21] In general, a higher coherence length is consistent with a structure comprising a low grain boundary density. Furthermore, a high coherence length is typically related to reduced charge trapping in the thin films, showing improved in-plane charge transport.[3,9d] The coherence length in the out-of-plane direction similarly affects charge transport. This is mainly because charge carriers are injected from the metal electrode into the OSC and are transported through the bulk film to the OSC/dielectric interface. As shown in Figure 4e, the coherence length of (001) is ≈34.6 nm for films cast at the speed of 0.1 mm s^{-1} and the gap distance of 0.05 mm. The value drops to ≈23.7 nm for 1.00 mm and ≈28.2 nm for

**ADVANCED
SCIENCE NEWS**

www.advancedsciencenews.com

**ADVANCED
FUNCTIONAL
MATERIALS**

www.afm-journal.de

Figure 5. The transfer curves are shown for 0.1 a) and 0.6 mm s^{-1} b) at the gap distances d of 0.05, 1.00, and 2.00 mm. OFET performance as a function of d for $v = 0.1$ mm s^{-1} with c) saturation mobility μ_{sat} (together with 0.6 mm s^{-1}), d) threshold voltage V_{th} and I_{on}/I_{off} ratio, e) reliability factor r_{sat} and effective mobility μ_{eff} and f) trap density N_t. All the measurements were performed at $V_{ds} = -40.0$ V for (a) and (b). The red-dashed line in Figure 5d–f indicates the morphology transition from type II → I. The error bars in Figure 5d–f are the standard deviation of over 15 device analysis.

2.00 mm. A similar trend is observed for 0.6 mm s^{-1}, whereby lower coherence lengths were calculated in comparison to the speed of 0.1 mm s^{-1}. The coherence length calculations indicate that a higher molecular order and larger crystallite size for the type II morphology has been achieved at an optimized meniscus (Figure 2).

The charge carrier transport of the zone-cast films was evaluated in field-effect transistors with a bottom-gate top-contact (BGTC) device configuration. As top contact electrode, 50 nm thick Au was used. The transistor analyses were completed for over 15 devices for each processing condition. More details regarding transistor characterization can be found in the Experimental Section. The transfer curves are compared in **Figure 5a,b** for variable gap distances and coating velocities representing the morphologies type II) at 0.05 mm and I) at 1.00 and 2.00 mm for 0.1 mm s^{-1}; and III) at 1.00 and 2.00 mm and IV) at 0.05 mm for 0.6 mm s^{-1}. The parameter sets were carefully chosen by design of experiments to prove the correlation between processing conditions and the charge carrier transport. The below analysis of the results proves that the number of data points is sufficient and the relation between electronic properties and processing parameters can be well explained by the structural analysis from GIWAXS and UV–vis. The comparison discloses the highest drain-source I_{ds} current in the saturation region for the type II morphology. The saturation mobility μ_{sat} for both coating speeds decreases with increasing d (Figure 5c). At $v = 0.1$ mm s^{-1}, the mobility decreases from 0.51 cm^2 V^{-1} s^{-1} for $d = 0.05$ mm to 0.15 cm^2 V^{-1} s^{-1} for $d = 2.00$ mm. This reduction in the charge carrier mobility is explained by the irregularities in morphology type I (Figure 2) due to the stick-slip motion of the meniscus

and a high grain boundary density (Figure 4e). For a coating speed of 0.6 mm s^{-1}, the charge carrier mobility drops by more than a factor of two from 0.22 cm^2 V^{-1} s^{-1} to 0.08 cm^2 V^{-1} s^{-1} by increasing d from 0.05 to 2.00 mm (Figure 5c). Although the crystallite size (Figure 4e) is in a similar range for $v = 0.1$ and 0.6 mm s^{-1}, the charge carrier mobility is decreased for the type III and IV morphologies due to crystal grain misalignment (Figure 2). More details on the output characteristics can be found in Section 4, Figure S6 (Supporting Information).

Figure 5d–f exhibits the device analysis for $v = 0.1$ mm s^{-1} and different gap distances. The threshold voltage V_{th} in Figure 5d is comparable for morphology types I and II. On the other hand, the I_{on}/I_{off} ratio slightly decreases from $\approx 2.6 \times 10^5$ to $\approx 7.2 \times 10^4$, similar to the charge carrier mobility. The highest and the average charge carrier mobilities are determined to be 0.80 and 0.51 cm^2 V^{-1} s^{-1} for morphology type II (Figure 5c). The saturation mobility of the zone-cast TIPS-pentacene films in our work is comparable to previously reported values.[3,10] Nevertheless, the non-ideal transfer curves may generally result in an overestimation of the calculated mobility. For this reason, we also determined the reliability factor r_{sat} and effective mobility μ_{eff} as a function of d presented in Figure 5e.[22] The morphology type II shows a good reliability factor of $r_{sat} = 62\%$. A more detailed explanation can be found in Section S4 (Supporting Information). Furthermore, the trap density N_t is calculated from the subthreshold swing SS based on the following equation[23];

$$SS = \frac{k_B T \ln 10}{q} \left[1 + \frac{q^2}{C_i} N_t \right] \quad (1)$$

with k_B the Boltzmann constant, T the absolute temperature, q the elementary charge, N_t the trap density (per unit area and unit energy) and C_i the insulator capacitance. As shown in Figure 5f, N_t exhibits a modest decrease from morphology type I to II. Morphology type II exhibits the lowest trap density with $N_t = 5 \times 10^{12}$ eV^{-1} cm^{-2} with respect to $N_t = 7 \times 10^{12}$ eV^{-1} cm^{-2} obtained for Morphology I. Although the change in N_t is minor, the trend is in agreement with the saturation mobility μ_{sat}. Hence, morphology type II results in an improved electrical behavior in OFETs, as evidenced by the enhanced film morphology and coherence length.

3. Conclusion

In conclusion, we investigated the role of the meniscus shape, controlled by the gap distance between the coating head and substrate, as well as by the coating velocity, on the morphology formation of zone-cast TIPS-pentacene. Four morphological subregimes are found and explained by fluid dynamics in the meniscus: I) stick-slip morphology, II) unidirectionally aligned crystals, III) spherulitic morphology, and IV) directional branched structure. Type II morphology provides improved crystallite size, saturation, and effective mobilities as well as reduced trap density in the thin films. Numerical simulation of the fluid dynamics provides insights into the concentration and temperature gradients responsible for the morphological transitions. The enhanced concentration gradient and minimum temperature difference in the front meniscus explain the formation of type II morphology and trigger a higher crystal alignment and structure homogeneity. Finally, this work provides fundamental understanding of the role of the meniscus shape on the film morphology during zone-casting, which is important for scaling-up any MGC technique for the deposition of functional layers for practical applications, especially in electronics.

4. Experimental Section

Materials and Substrate Preparation: All solvents, TIPS-pentacene, and PETS were purchased from Sigma–Aldrich and used as received. Highly doped silicon substrates with a 300 nm thick SiO$_2$ layer were cleaned in an ultrasonic bath by using acetone (10 min) and isopropyl alcohol (5 min) and dried with N$_2$ gas. After exposure to oxygen plasma for 10 min, the surface was treated with trichloro(phenethyl)silane (PETS) in a vacuum oven heated at 140 °C and vacuumed to 10 mbar for 3 h.

Zone-Casting Experiments: Zone-casting experiments were performed with a specially designed setup. The gap distance d between the coating head and the substrate was set to 0.05, 0.25, 1.00, 1.50, and 2.00 mm. The solution and the substrate were heated at 45 °C. A flow rate of ≈ 2 μL s^{-1} was set to keep the meniscus shape during film deposition constant. The substrate speed ranged from 0.1 to 0.6 mms^{-1}. Before starting each deposition run, an initial meniscus of ≈ 0.15 mL was established.

Morphological Characterization and GIWAXS Measurements: Film thickness measurements were performed by a KLA Tencor Profilometer. Optical microscopy images were obtained by a Leica Light Microscope in reflection. AFM studies were executed using Dimension Fast Scan by Bruker in tapping mode. Grazing incidence wide-angle X-ray scattering (GIWAXS) measurements were performed at the Max Planck Institute for Polymer Research. The photon energy was set to 10 keV ($\lambda = 1.24$ Å). The sample chamber was vacuumed to ≈ 1 mbar during the measurement. The incident angle (α_i) of the X-ray beam was adjusted individually for each sample in the range of 0.19°–0.20°. The scattered intensity was recorded by a 2D image plate (MAR345, marXperts GmbH, Norderstedt, Germany). The exposure time was 180 s. The q-range ($q = 4\pi \sin\theta \ \lambda^{-1}$) was cali-

brated using a silver behenate standard. The data were processed and analyzed using Datasqueeze (University of Pennsylvania, Philadelphia, PA, USA) and OriginPro (OriginLab Corporation, Northampton, MA, USA).

Transistor Fabrication and Characterization: BGTC device configuration was used for OFETs. TIPS-pentacene was dissolved in THF at a concentration of 1 mg mL^{-1}. After the zone-casting of the active layer, a 50 nm thick Au layer was deposited at an evaporation rate of 1 Å s^{-1}. The channel length of the electrode geometry was 30 μm, and the width of the electrodes was 1000 μm. Afterward, the devices were annealed at 50 °C for 12 h in a N$_2$-filled glove box. Electrical characterizations were done using Keithley 4200-SCS in a N$_2$-filled glove box. Field-effect mobilities were calculated in the saturation regime using conventional transconductance analysis given by $\mu_{FET} = (2L/W)(1/C_i)(\partial\sqrt{I_D}/\partial V_G)^2$. Measurements were performed for V_G sweeping from 10 to −40 V at a constant $V_D = -40$ V.

Supporting Information

Supporting Information is available from the Wiley Online Library or from the author.

Conflict of Interest

The authors declare no conflict of interest.

Data Availability Statement

The data that support the findings of this study are available from the corresponding author upon reasonable request.

[1] a) Y. Diao, L. Shaw, Z. Bao, S. C. B. Mannsfeld, *Energy Environ. Sci.* **2014**, *7*, 2145; b) Z. Chai, S. A. Abbasi, A. A. Busnaina, *ACS Appl. Mater. Interfaces* **2018**, *10*, 18123; c) H. Sirringhaus, *Adv. Mater.* **2014**, *26*, 1319.

[2] J. J. Michels, K. Zhang, P. Wucher, P. M. Beaujuge, W. Pisula, T. Marszalek, *Nat. Mater.* **2020**, *20*, 68.

[3] G. Giri, E. Verploegen, S. C. B. Mannsfeld, S. Atahan-Evrenk, D. H. Kim, S. Y. Lee, H. A. Becerril, A. Aspuru-Guzik, M. F. Toney, Z. Bao, *Nature* **2011**, *480*, 504.

[4] X. Gu, L. Shaw, K. Gu, M. F. Toney, Z. Bao, *Nat. Commun.* **2018**, *9*, 534.

ADVANCED
SCIENCE NEWS

www.advancedsciencenews.com

ADVANCED
FUNCTIONAL
MATERIALS

www.afm-journal.de

[5] J.-C. Lee, M. Lee, H.-J. Lee, K. Ahn, J. Nam, S. Park, *Adv. Mater.* **2020**, *32*, 2004864.

[6] K. Zhang, Z. Wang, T. Marszalek, M. Borkowski, G. Fytas, P. W. M. Blom, W. Pisula, *Mater. Horiz.* **2020**, *7*, 1631.

[7] A. Perez-Rodriguez, I. Temino, C. Ocal, M. Mas-Torrent, E. Barrena, *ACS Appl. Mater. Interfaces* **2018**, *10*, 7296.

[8] W. Pisula, A. Menon, M. Stepputat, I. Lieberwirth, U. Kolb, A. Tracz, H. Sirringhaus, T. Pakula, K. Müllen, *Adv. Mater.* **2005**, *17*, 684.

[9] a) M. Chen, B. Peng, S. Huang, P. K. L. Chan, *Adv. Funct. Mater.* **2020**, *30*, 1905963; b) R. Janneck, F. Vercesi, P. Heremans, J. Genoe, C. Rolin, *Adv. Mater.* **2016**, *28*, 8007; c) J.-C. Lee, J.-O. Kim, H.-J. Lee, B. Shin, S. Park, *Chem. Mater.* **2019**, *31*, 7377; d) O. Yildiz, Z. Wang, M. Borkowski, G. Fytas, P. W. M. Blom, J. J. Michels, W. Pisula, T. Marszalek, *Adv. Funct. Mater.* **2022**, *32*, 2107976; e) K. Zhang, M. Borkowski, P. Wucher, P. M. Beaujuge, J. J. Michels, P. W. M. Blom, T. Marszalek, W. Pisula, *Adv. Electron. Mater.* **2021**, *7*, 2100397; f) K. Zhang, T. Marszalek, P. Wucher, Z. Wang, L. Veith, H. Lu, H. J. Räder, P. M. Beaujuge, P. W. M. Blom, W. Pisula, *Adv. Funct. Mater.* **2018**, *28*, 1805594.

[10] R. Janneck, D. Karagiannis, P. Heremans, J. Genoe, C. Rolin, *Adv. Mater. Interfaces* **2019**, *6*, 1900614.

[11] Y. Diao, B. C.-K. Tee, G. Giri, J. Xu, D. H. Kim, H. A. Becerril, R. M. Stoltenberg, T. H. Lee, G. Xue, S. C. B. Mannsfeld, Z. Bao, *Nat. Mater.* **2013**, *12*, 665.

[12] R. Janneck, P. Heremans, J. Genoe, C. Rolin, *Adv. Mater. Interfaces* **2018**, *5*, 1800147.

[13] P. Born, S. Blum, A. Munoz, T. Kraus, *Langmuir* **2011**, *27*, 8621.

[14] a) M. Le Berre, Y. Chen, D. Baigl, *Langmuir* **2009**, *25*, 2554; b) L. L. B. Levich, *Acta Physicochim.* **1942**, *17*, 141.

[15] a) T. Izawa, E. Miyazaki, K. Takimiya, *Adv. Mater.* **2008**, *20*, 3388; b) J. H. Lee, Y. Seo, Y. D. Park, J. E. Anthony, D. H. Kwak, J. A. Lim, S. Ko, H. W. Jang, K. Cho, W. H. Lee, *Sci. Rep.* **2019**, *9*, 21.

[16] S. Kwon, J. Kim, G. Kim, K. Yu, Y.-R. Jo, B.-J. Kim, J. Kim, H. Kang, B. Park, K. Lee, *Adv. Mater.* **2015**, *27*, 6870.

[17] F. Doumenc, B. Guerrier, *Europhys. Lett.* **2013**, *103*, 14001.

[18] Z. Zhang, B. Peng, X. Ji, K. Pei, P. K. L. Chan, *Adv. Funct. Mater.* **2017**, *27*, 1703443.

[19] C. Ramanan, A. L. Smeigh, J. E. Anthony, T. J. Marks, M. R. Wasielewski, *J. Am. Chem. Soc.* **2012**, *134*, 386.

[20] Y. Yuan, G. Giri, A. L. Ayzner, A. P. Zoombelt, S. C. B. Mannsfeld, J. Chen, D. Nordlund, M. F. Toney, J. Huang, Z. Bao, *Nat. Commun.* **2014**, *5*, 3005.

[21] B. D. C. S. R. Stock, *Elements of X-ray Diffraction*, Prentice-Hall Inc, Upper Saddle River, New Jersey **2001**.

[22] H. H. Choi, K. Cho, C. D. Frisbie, H. Sirringhaus, V. Podzorov, *Nat. Mater.* **2017**, *17*, 2.

[23] W. L. Kalb, B. Batlogg, *Phys. Rev. B* **2010**, *81*, 035327.